# nature physics

**Article** 

https://doi.org/10.1038/s41567-023-02209-x

# Bogoliubov quasiparticle on the gossamer Fermi surface in electron-doped cuprates

Received: 17 May 2023

Accepted: 8 August 2023

Published online: 25 September 2023



Ke-Jun Xu<sup>1,2,3,16</sup>, Qinda Guo <sup>4,16</sup>, Makoto Hashimoto <sup>5,16</sup>, Zi-Xiang Li<sup>6,7,16</sup>, Su-Di Chen <sup>1,2,3,15</sup>, Junfeng He <sup>1,2,8</sup>, Yu He <sup>1,2,3,9</sup>, Cong Li <sup>3,4</sup>, Magnus H. Berntsen <sup>4</sup>, Costel R. Rotundu <sup>1,2</sup>, Young S. Lee <sup>1,2,3</sup>, Thomas P. Devereaux <sup>1,2,10</sup>, Andreas Rydh <sup>1,1</sup>, Dong-Hui Lu <sup>5</sup>, Dung-Hai Lee <sup>1,2,3,14</sup> ○ Oscar Tjernberg <sup>4</sup> ○ & Zhi-Xun Shen <sup>1,2,3,14</sup>

Electron-doped cuprates consistently exhibit strong antiferromagnetic correlations, leading to the prevalent belief that antiferromagnetic spin fluctuations mediate Cooper pairing in these unconventional superconductors. However, early investigations showed that although antiferromagnetic spin fluctuations create the largest pseudogap at hot spots in momentum space, the superconducting gap is also maximized at these locations. This presented a paradox for spin-fluctuation-mediated pairing: Cooper pairing is strongest at momenta where the normal-state low-energy spectral weight is most suppressed. Here we investigate this paradox and find evidence that a gossamer—meaning very faint—Fermi surface can provide an explanation for these observations. We study Nd<sub>2-r</sub>Ce<sub>r</sub>CuO<sub>4</sub> using angle-resolved photoemission spectroscopy and directly observe the Bogoliubov quasiparticles. First, we resolve the previously observed reconstructed main band and the states gapped by the antiferromagnetic pseudogap around the hot spots. Within the antiferromagnetic pseudogap, we also observe gossamer states with distinct dispersion, from which coherence peaks of Bogoliubov quasiparticles emerge below the superconducting critical temperature. Moreover, the direct observation of a Bogoliubov quasiparticle permits an accurate determination of the superconducting gap, yielding a maximum value an order of magnitude smaller than the pseudogap, establishing the distinct nature of these two gaps. We propose that orientation fluctuations in the antiferromagnetic order parameter are responsible for the gossamer states.

The Bardeen–Cooper–Schrieffer (BCS) theory of superconductivity successfully explains the pairing and condensation of quasiparticles in conventional superconductors, where the attractive potential that binds the electrons into Cooper pairs, arises from the exchange of lattice vibrations or phonons. However, in unconventional superconductors like cuprates, the pairing glue is thought to arise from the electrons themselves through electron–electron interactions  $^{2-5}$ . This means

that the electrons simultaneously act to glue and to be glued. An early discussion on the challenge of the dual roles is given elsewhere  $^6$ .

Because the parent compounds of the cuprates are antiferromagnetic (AF) insulators and superconductivity arises after the demise of the AF long-range order  $^7$ , from early on, it has been proposed that AF spin fluctuations are an important source of Cooper pairing in cuprate superconductors. In addition to cuprates, other materials where AF

A full list of affiliations appears at the end of the paper. 🖂 e-mail: dunghai@berkeley.edu; oscar@kth.se; zxshen@stanford.edu

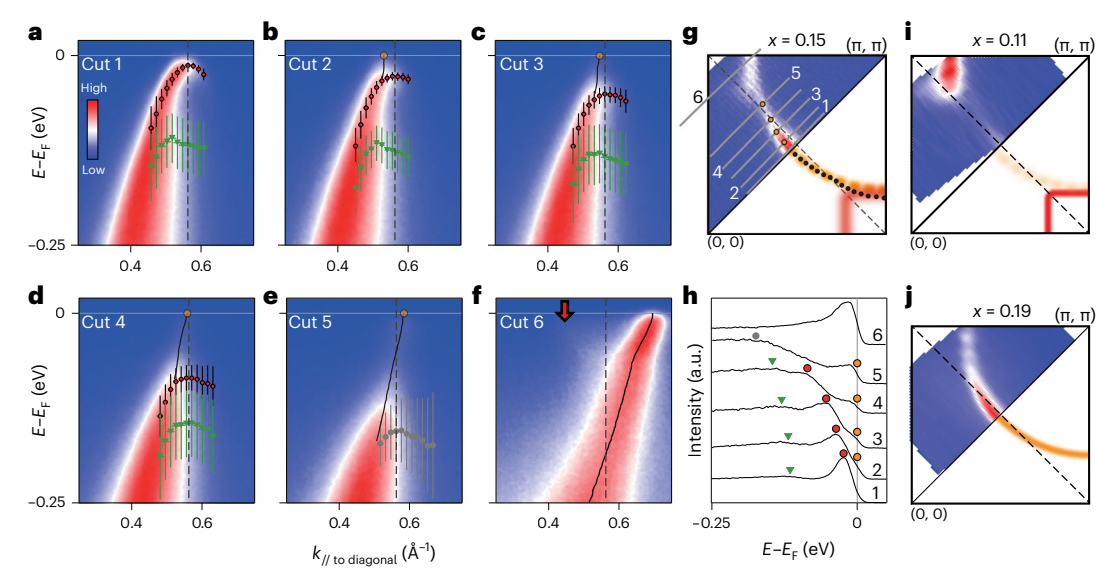


**Fig. 1**| **Momentum-dependent normal-state electronic structure of NCCO. a**–**f**, Energy–momentum spectra corresponding to the numbered cuts in **g**. The red dots track the position of the peak associated with the AF pseudogap and the green triangles track a higher-energy hump feature (see the main text). The grey dots in **e** track the only observable broad feature in this cut. The black lines in **a**–**e** track the dispersion from fitting the momentum distribution curves (MDCs) at binding energies within the pseudogap in cuts 1–5. Cut 6 passes through the reconstructed electron pocket centred at (0, π), and the black line tracks the MDC peaks for the entire energy range shown here. The vertical black dashed line indicates the AF zone boundary. The red arrow in **f** highlights the weak ( $\pi$ ,  $\pi$ )-folded dispersion branch near the AF zone boundary. Error bars in **a**–**e** correspond to the width of peaks in the energy distribution curves (EDC) fittings. **g**, Fermi surface mapping (upper left half) taken by integrating 10 meV of spectra within the Fermi level. The lower right half is a schematic indicating the existence of both the gossamer Fermi surface (orange) and reconstructed

Fermi surface (red). The black dashed diagonal line indicates the AF zone boundary. The grey numbered lines indicate the momentum cuts for  $\mathbf{a}-\mathbf{f}$ . The black dots overlaid in the bottom-right half are the experimentally extracted  $k_{\rm F}$  values from the MDC peaks.  $\mathbf{h}$ , EDCs at the Fermi momentum ( $k_{\rm F}$ ) for cuts 1–6. The black arrow highlights the Fermi surface crossing of the states within the AF pseudogap. The curves are vertically offset for clarity. The orange dots in  $\mathbf{a}-\mathbf{h}$  highlight the  $k_{\rm F}$  positions of the gossamer states.  $\mathbf{i}$ , Fermi surface mapping of an 11% doping sample, showing the strong intensity of the reconstructed electron pocket in the Brillouin zone boundary.  $\mathbf{j}$ , Fermi surface mapping of a 19% doping sample, showing a full large pocket. The extremely overdoped regime is achieved by surface K dosing, and the doping level is estimated from the Fermi surface volume. Data for the 15% sample are taken at the MAX IV Bloch beamline. Data for the 11% and 19% samples are taken at SSRL beamline 5-4. The measurement temperature for  $\mathbf{a}-\mathbf{g}$  is around 25 K, and that for  $\mathbf{i}$  and  $\mathbf{j}$  is 7 K.

is suspected to play an important role in pairing include iron-based superconductors, heavy-fermion superconductors and organic superconductors  $^{3-5}$ . Therefore, acquiring a comprehensive understanding of the mechanism behind AF spin fluctuations is essential in unconventional superconductivity research.

For hole-doped cuprates, spin fluctuation exchange is predicted to cause the d-wave pairing symmetry $^2$ , which is confirmed by experiments $^{8,9}$ . However, due to the presence of a pseudogap $^{10-13}$ , multiple competing ordering tendencies $^{14-19}$ , Van Hove singularity $^{20}$  and phenomena associated with antinodal  $B_{1g}$  phonon coupling $^{21-23}$ , an unambiguous identification of the pairing mechanism remains a daunting task. The situation is notably different in the electron-doped cuprates—AF correlation is much stronger than any other ordering tendencies $^7$ . This makes them excellent model systems to study the spin fluctuation pairing mechanism.

# $Nd_{1.85}Ce_{0.15}CuO_4$ as a model system

The magnetic and electronic properties of the electron-doped cuprates have been extensively investigated  $^7$ . Compared with the hole-doped side, the long-range AF order persists over a broader doping range on the electron-doped side  $^{7,24}$ . Furthermore, the AF remains commensurate at  $(\pi,\pi)$  with doping  $^{25,26}$ , in contrast to stripe-ordered hole-doped materials  $^{14}$ .

Previous electronic structure studies using angle-resolved photoemission spectroscopy (ARPES) have identified an incipient spectral reconstruction in the form of a  $(\pi,\pi)$  folding<sup>27</sup>, even when the sample has no long-range AF order near optimal doping<sup>28</sup>. In addition, the material exhibits an AF pseudogap<sup>29–33</sup>, which gradually fills as a function of

doping in the range where superconductivity appears<sup>34</sup>. In the superconducting state, previous studies used the leading-edge shift in the ARPES spectra to infer the superconducting gap  $\Delta_{sc}$  (refs. 35–39), since the coherence peak was not observed. There are conflicting results on the momentum dependence of  $\Delta_{SC}$ : an earlier study suggests that  $\Delta_{SC}$ exhibits a maximum near the hot-spot momenta<sup>35</sup>, consistent with a Raman study<sup>40</sup>, whereas other ARPES studies show a simple d-wave form<sup>38,39</sup>. Furthermore, there is a debate as to whether the putative maximum in the leading-edge shift is solely due to superconductivity<sup>41</sup>, as the presence of the pseudogap at the hot spots makes the determination of the superconducting gap through the leading-edge shift unreliable. The absence of the superconducting coherence peaks in ARPES measurements has, thus far, prevented the positive identification of superconductivity-related states. The conflicting results and interpretations in the literature, as well as our desire to solve the pairing dilemma outlined in the abstract, lead us to carry out a comprehensive investigation of this material.

In the following, we study the electronic properties of  $Nd_{1.85}Ce_{0.15}CuO_4$  (NCCO) in both normal and superconducting states. We begin by examining the normal-state electronic structure of NCCO, focusing on the presence of the AF pseudogap near the hot spots. Owing to the much-improved experimental conditions and sample preparation processes (Methods), we were able to observe faint dispersive features inside the AF pseudogap, which form the gossamer Fermi surface, as well as the emergence of Bogoliubov quasiparticles from these states below the superconducting transition temperature ( $T_c$ ). The observation of the superconducting coherence peak allows us to ascertain the intrinsic nature of these

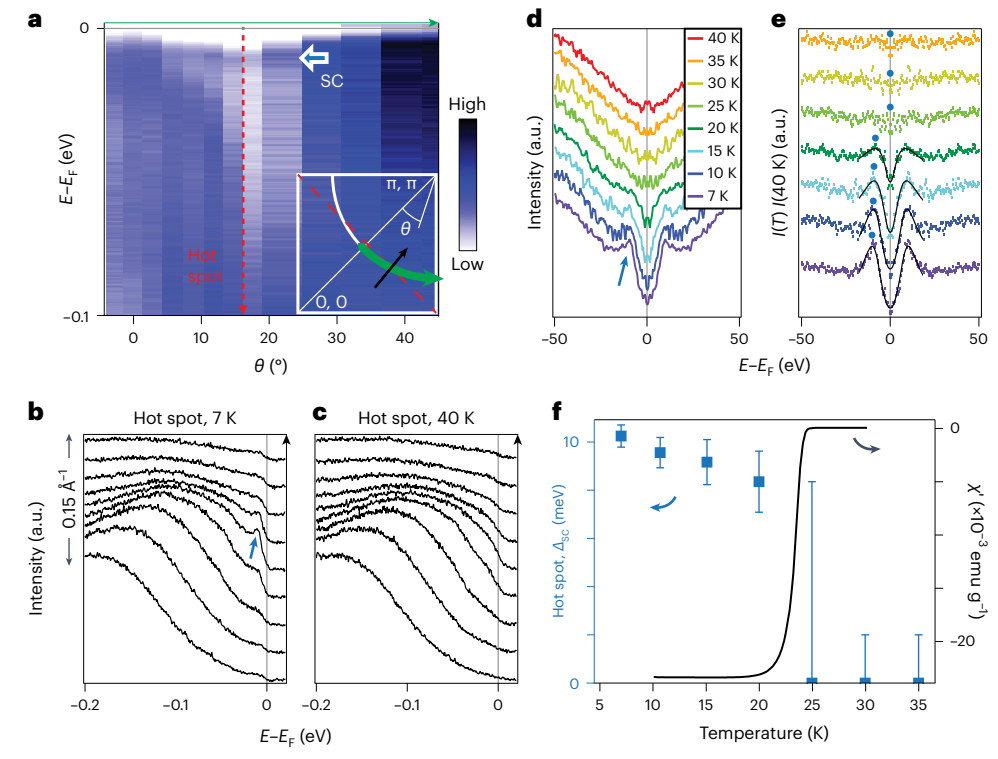


**Fig. 2** | **Temperature-dependent spectra reveal the origin of the low-energy peak. a**, Colour-scale plot of the raw EDCs in the superconducting state along an arc on the large Fermi surface (indicated by the green arrow in the inset). The blue arrow highlights the low-energy peak feature. The red vertical dashed line and arrow indicate the approximate location of the hot spot. Intensity values are normalized by the angle-dependent photoemission matrix element extracted from the overdoped NCCO spectra, which is minimally affected by AF (Extended Data Fig. 4). Measurement temperature, 7 K. b. c, EDCs of a cut across the hot spot (indicated by the black arrow in the inset of **a**) at 7 K (**b**) and 40 K (**c**). The cut direction is shown by the black arrows beside the panels corresponding to the black arrow in the inset of **a**. The blue arrow highlights the low-energy peak

feature. **d**, Temperature dependence of the EDCs at the hot spot  $k_{\rm F}$  for different temperatures corresponding to the coloured legend in the inset. The blue arrow highlights the low-energy peak feature. **e**, Temperature dependence of EDCs normalized by the 40 K spectrum. The black line is the phenomenological fit (Methods) with a constant background. The blue dots highlight the superconducting gap edge. **f**, Extracted superconducting gap  $(\chi)$  as a function of temperature (left). The vertical error bars correspond to the variance in the fitted gap values with different starting parameters multiplied by a factor of 2. The uncertainty in temperature is smaller than the data point size. Temperature-dependent magnetic susceptibility (right). Curves in **b**-**e** are vertically offset for clarity. Data are taken at SSRL beamline 5-4.

in-gap states and to accurately measure the superconducting gap size. The result of these measurements establishes the presence and importance of two sectors of state, providing a route to reconcile the dilemma of the maximum superconducting gap occurring where the normal-state spectral weight is suppressed the most. Finally, we present a theoretical proposal that explains the experimental observations. By combining these experimental and theoretical approaches, we provide a comprehensive picture of the inner workings of AF spin fluctuations.

# Normal-state electronic structure

We first investigate how short-range antiferromagnetism affects the electronic structure of NCCO in the absence of superconductivity. Figure 1a-f shows the momentum dependence of the electronic structure of NCCO at x=0.15 in the normal state. Despite the lack of long-range AF order at this doping level<sup>28</sup>, we observe distinct signatures of electronic structure reconstruction (red dots in cuts 1-4 and red arrow in cut 6; Extended Data Figs. 1 and 2 provide the details and data fitting) near the AF zone boundary, consistent with previous studies<sup>27</sup>. This reconstruction refers to the  $(\pi, \pi)$  folding of the electronic states. We also observe a dispersion anomaly (Fig. 1, green dots) at higher binding energies, which may be attributed to electron–phonon coupling in view of its energy scale<sup>42</sup>. Towards the zone boundary, the two features (Fig. 1, red and green dots) become broad and merge into a single broad peak (Fig. 1e,h), probably due to increased scattering

rates<sup>27</sup>. In the following, by the AF pseudogap feature, we refer to the dispersion anomaly (Fig. 1, red dots) that bends back the main band. We leave the mechanism responsible for the green dots (Fig. 1) and its implications for an upcoming study.

Most importantly, we can extract a well-defined dispersion (black traces in Fig. 1a–e are obtained by fitting the momentum distribution curves; Extended Data Fig. 3) within the AF pseudogap and observe a clear Fermi level ( $E_{\rm F}$ ) crossing (Fig. 1h, orange dots) despite the existence of the AF pseudogap. This feature suggests the persistence of a gossamer large Fermi surface within the AF pseudogap (red dots). In Fig. 1g, we highlight the gossamer Fermi surface in orange. Apparently, it approximates the large Fermi surface without the AF reconstruction. Near the Brillouin zone boundary, we also observe both reconstructed and unreconstructed states, supporting the existence of a gossamer band. Nonetheless, we note that other factors such as an anisotropic scattering rate may play a contributing role in shaping the spectra<sup>27</sup>.

For comparison, we also show the Fermi surfaces of an underdoped 11% sample (Fig. 1i) and an overdoped 19% sample (Fig. 1j), both with an absence of superconductivity. For the underdoped sample with long-range AF order, the Fermi surface is dominated by the reconstructed electron pocket centred at  $(0,\pi)$  with almost no states in the gossamer Fermi surface. For the overdoped sample with no spectral signature of AF, the gossamer Fermi surface has evolved into a full Fermi surface with a Fermi surface volume corresponding to 19% doping.

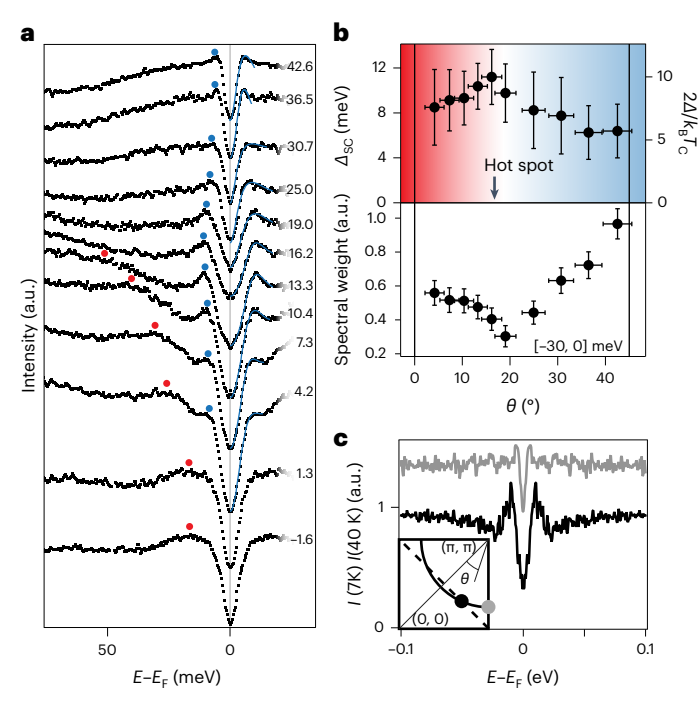


Fig. 3 | Momentum dependence of Bogoliubov quasiparticles, a. Momentum dependence of the  $k_{\rm F}$  spectra along an arc on the large Fermi surface. The red dots track the peak feature related to the AF pseudogap, and the blue dots track the low-energy Bogoliubov quasiparticle peak. Numbers to the right indicate the angle away from the Brillouin zone diagonal, with angle  $\theta$  defined in the inset of c. The blue curves overlaying the EDC data in the symmetrized part above  $E_{\rm F}$  are the phenomenological fits of the superconducting gap (Methods). A secondorder background was used to capture the normal-state background spectral weight. Curves near  $\theta = 0$  were not fitted as the large size of the AF pseudogap overshadows any small superconducting gap that may be present within. **b**, Momentum dependence of  $\Delta_{SC}$  and the corresponding  $2\Delta_{SC}/k_BT_c$  ratios measured at 7 K (top). The black vertical arrow indicates the approximate location of the hot spot. The gap data near the Brillouin zone diagonal is not available due to the dominance of the AF pseudogap. The red background highlights the dominance of AF on the low-energy spectra near  $\theta = 0$ , and the blue background highlights the dominance of superconductivity near  $\theta$  = 45. The error bars correspond to the variance in the fitted gap values with different starting parameters multiplied by a factor of 2. Integrated spectral weight in the range of [-30, 0] meV (bottom). The intensity values are normalized by the angledependent photoemission matrix element extracted from the overdoped NCCO spectra. The vertical error bars correspond to the noise range in the spectra multiplied by the integration area. The horizontal error bars correspond to the uncertainty in the absolute momentum determination. c, EDCs at the hot spot (black) and Brillouin zone boundary (grey) at 7 K for the same sample, normalized by the respective spectra at 40 K. The Brillouin zone location of EDCs is shown in the inset. The Brillouin zone boundary curve is vertically offset by 0.2 for clarity.

# **Bogoliubov quasiparticles**

After obtaining a clear picture of the electronic structure in the normal state, we proceeded to investigate the superconducting state. Figure 2a displays the raw data of the ARPES spectra along an arc on the unreconstructed large Fermi surface. It is noteworthy that a low-energy spectral feature appears at around 10 meV below  $E_{\rm F}$  (Fig. 2a, blue arrow). The binding energy of this feature reaches a maximum near the hot spot. We note that the intensity as a function of the Fermi surface angle is normalized by the matrix element obtained from the overdoped spectra (Extended Data Fig. 4). To further examine this low-energy feature, Fig. 2b,c shows a cut through the hot spot at temperatures below (7 K) and above (40 K) the  $T_{\rm c}$  value of 25 K. A coherence peak (Fig. 2d, blue arrow) is clearly visible at 7 K and disappears at 40 K. Figure 2d,e further demonstrates the detailed temperature dependence of the

symmetrized energy distribution curves (EDCs) at the hot-spot Fermi momentum ( $k_{\rm F}$ ). The gap associated with the coherence peak closes at around 25 K. Figure 2f shows the extracted low-energy gap as a function of temperature, with the temperature-dependent magnetic susceptibility (black curve) also shown. These data unambiguously demonstrate that the coherence peak feature is associated with the Bogoliubov quasiparticle. From Fig. 2a, the largest superconducting gap of about 10 meV is about an order of magnitude smaller than the energy scale associated with the AF pseudogap spectral-weight suppression at the hot spot. To clarify the momentum dependence, we note that the AF pseudogap is particle—hole symmetric only at the hot spots. For momenta near the zone diagonal, the Fermi energy is closer to the lower branch of the gapped density of states. This explains why in Fig. 2a, the AF pseudogap has an apparent momentum-dependent gap edge.

After establishing the superconducting origin of the low-energy peak, we investigate its momentum dependence. Figure 3a shows the EDCs at  $k_{\rm F}$  on the electron pocket and along an arc of the gossamer Fermi surface, where we observe Bogoliubov quasiparticle peaks at most momenta (blue dots). However, near the zone diagonal ( $\theta \approx 0$ ), the identification of the presumed superconducting gap node is complicated by the presence of the AF pseudogap (Fig. 3a, red dots). The temperature dependence shown in Extended Data Fig. 5 corroborates the AF origin of the zone diagonal gap, which persists above the bulk  $T_{\rm c}$  of 25 K. It is important to note that the gapping of the node by AF has been observed in other electron-doped cuprates  $^{43,44}$ , but since it is derived from the AF pseudogap, this nodal gap did not invalidate the d-wave pairing symmetry.

The momentum dependence of  $\Delta_{\rm SC}$  is determined by fitting the low-energy gap using a phenomenological model (Methods). The extracted gap values are plotted in Fig. 3b (top), along with the corresponding low-energy spectral weight in the bottom panel. Despite the lowest normal-state spectral weight at the hot spot, it exhibits the largest  $\Delta_{\rm SC}$  of -11 meV, corresponding to  $2\Delta/k_{\rm B}T_{\rm c}\approx 10$  and displays a prominent Bogoliubov quasiparticle peak (Fig. 3c). In contrast, at the zone boundary, where the  $(\pi,\pi)$  folding leaves a reconstructed Fermi surface in the normal state (Fig. 1f), we observe a  $\Delta_{\rm SC}$  of ~6 meV, corresponding to  $2\Delta/k_{\rm B}T_{\rm c}\approx 5$ , slightly larger than the weak-coupling BCS value¹. Furthermore, the Bogoliubov quasiparticle peak at the hot spot is much more evident than that at the zone boundary after normalization (Fig. 3c). These results definitively explain the dilemma discussed earlier—the superconducting gap appears on the gossamer Fermi surface inside the normal-state AF pseudogap.

We have also performed specific heat measurements (Extended Data Fig. 6) that reveal a small superconducting transition anomaly compared with the expected BCS value derived from the bare-band structure. This is comparable with the small specific heat anomaly in previous measurements at similar doping<sup>45</sup> and consistent with the low spectral weight on the gossamer Fermi surface from which superconductivity arises. Methods provides details of the calorimetry measurements.

Before presenting our theoretical findings, it is reasonable to question whether the coexistence of AF reconstruction plus the pseudogap and gossamer large Fermi surface within the pseudogap can be due to mesoscale separation into an AF-ordered phase and a metallic phase with a large Fermi surface. In Methods and Extended Data Fig. 7, we present reasons for why this scenario is unlikely. This has motivated us to search for other origins of the in-gap states, discussed in the following.

## **Spin orientational fluctuations**

Our approach to understand the AF pseudogap and the states inside it is based on the concept that the AF order parameter has a modulus and an orientation. The modulus creates the pseudogap and the reconstruction of the electronic structure, whereas the orientation fluctuation removes the AF long-range order and restores states inside

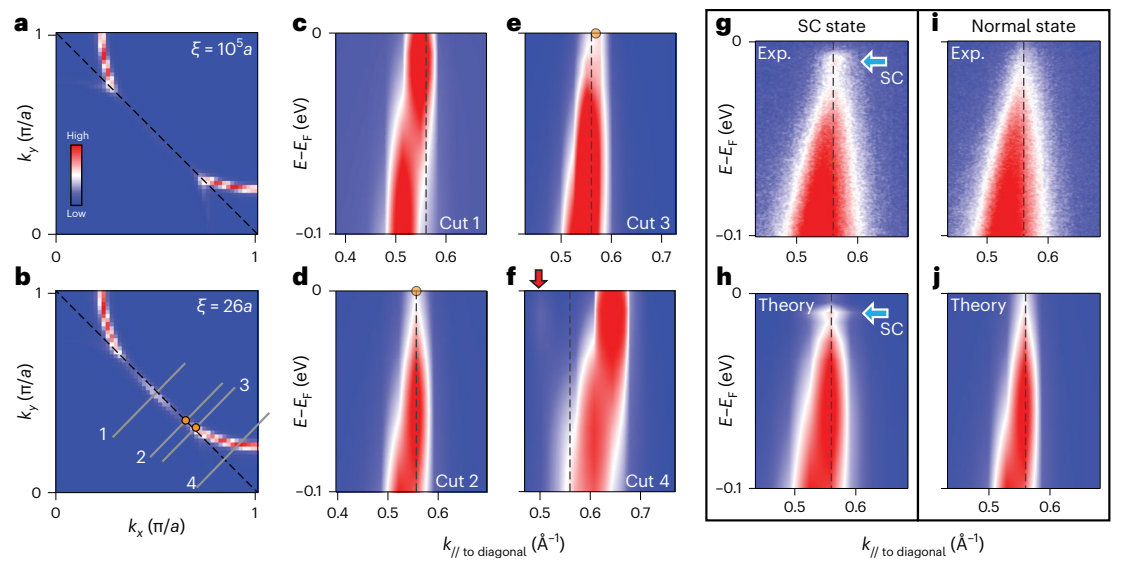


**Fig. 4** | **Spin orientational fluctuations restore gossamer states. a,b**, Calculated Fermi surfaces at AF correlation lengths  $\xi_{AF}$  of  $10^5a$  (**a**) and 26a (**b**), where a is the lattice constant. **c-f**, Calculated spectra of cuts indicated by the grey lines in **b**. The red arrow above cut 4 highlights the reconstructed feature near the AF zone boundary. The orange dots highlight the presence of the gossamer Fermi surface within the AF pseudogap. **g,h**, Experimental (**g**) and

calculated (h) spectra in the superconducting (SC) state. The calculated superconducting spectra is obtained by real-space Cooper pairing.

i.j. Experimental (i) and calculated (j) spectra in the normal state. The blue arrows in g and h highlight the coherence peak of the Bogoliubov quasiparticle.

The black dashed lines in all the panels indicate the AF zone boundary.

the pseudogap. This proposal is very similar to that proposed in another work  $^{46}$  to account for the states inside the AF pseudogap at the hot spot. This assumption is consistent with previous neutron scattering studies  $^{47-49}$ , where the low-energy slow spin fluctuations show a nearly constant total moment with doping but a gradual diffusion of spectral weight into inelastic channels. Unlike that in the other work  $^{46}$ , the goal of our theoretical model is to show that the AF spin orientation fluctuations can restore the gossamer Fermi surface—the large Fermi surface without AF reconstruction—as well as to show that Cooper pairing can occur on this gossamer Fermi surface.

To test this hypothesis, we carry out numerical simulations under the assumption that the orientation fluctuation occurs at a much slower timescale than the photoemission process. This allows us to calculate the ARPES spectra under different orientation configurations and then average over these configurations (2400 in total). These configurations were generated using the Boltzmann weight of a classical two-dimensional Heisenberg model with different correlation lengths (Methods).

Figure 4a,b shows the calculated Fermi surfaces at long and short correlation lengths ( $\xi_{AF}$ ) of the spin orientation. At  $\xi_{AF}$  much longer than the numerical system size (which is  $100 \times 100$  lattice sites), the Fermi surface appears reconstructed, with very low density of states at  $E_F$  near the hot spots and zone diagonals. As  $\xi_{AF}$  is reduced to about 25 lattice sites, comparable with the measured  $\xi_{AF}$  from neutron scattering experiments for this doping level and at low temperatures the states along the large Fermi surface are partially restored. We further analyse the energy—momentum spectra across different momenta (Fig. 4c-f). Although there is spectral reconstruction (red arrow) at the zone boundary (Fig. 4f), the incomplete spectral-weight suppression and the residual spectral weight within the AF pseudogap at the hot spot (Fig. 4d, cut 2) are evident.

In the above approach, the electrons are assumed to adiabatically follow the AF orientation fluctuation (analogous to the Born–Oppenheimer approximation for phonons). Cooper pairing is triggered by the breaking of this adiabaticity. We assume that after integrating out the fast orientation fluctuations, a short-range AF interaction

is generated, which mediates Cooper pairing. Here, to avoid a circular argument, Cooper pairing is implemented in the real space by nearest-neighbour *d*-wave pairing. Figure 4h shows the calculated superconducting ARPES spectra at the hot spot, where the coherence peak of the Bogoliubov quasiparticle within the AF pseudogap is evident. Comparing Fig. 4h,j with the experimental data in Fig. 4g,i, we observe a qualitative agreement. Methods provides additional details.

# Low-energy gossamer states drive coherent superconductivity

The totality of our results firmly establishes the existence of two sectors of states in superconducting NCCO-states reconstructed and pseudo-gapped by the AF correlations, and states forming the gossamer large Fermi surface within the AF pseudogap. Near the hot spots, these two sectors of states are well separated in energy. Here we observe the largest  $\Delta_{SC}$  and the most well-defined coherence peaks despite the most prominent spectral-weight depletion, suggesting that the states within the gossamer Fermi surface dominate pair formation. The remarkable emergence of coherent Bogoliubov quasiparticles from a phenomenologically incoherent spectra at the hot spot (Fig. 1h) suggests that there is a hidden coherent nature of the gossamer states. On the other hand, the reconstructed states and unreconstructed gossamer states near  $E_{\rm F}$  merge together towards the Brillouin zone boundary. It is an interesting open question as to how these states interact and lead to a small superconducting gap near the Brillouin zone boundary. One intriguing possibility is that the reconstructed electron pocket centred at  $(0, \pi)$  is proximitized by the strong-coupling superconductivity of the gossamer states within the AF pseudogap.

The notion that the gossamer states drive pair formation and phase-coherent superconductivity is consistent with the phase diagram of the electron-doped cuprates. In retrospect, the bulk-superconducting phase seemingly emerges with the appearance of the gossamer Fermi surface. On the underdoped side, the long-ranged AF order depletes almost all the states within the gossamer Fermi surface (Fig. 1i). On the overdoped side, the gossamer Fermi surface evolves into a full unreconstructed large Fermi surface (Fig. 1j).

Apparently, the pairing interaction due to spin fluctuations is diminished and the system is not superconducting (Extended Data Fig. 8). These observations suggest that the presence of a gossamer Fermi surface and strong spin fluctuations are required for bulk superconductivity in the electron-doped cuprates.

# Implications for strongly correlated superconductors

Our study of the electron-doped cuprates sheds light on the competition between the AF pseudogap and Cooper pairing within a single low-energy effective band. Specifically, the spin-1 electron-hole bound states participate in forming the AF order parameter, leaving the rest of the electrons on either the reconstructed Fermi surface or the gossamer large Fermi surface for pairing. A comprehensive understanding of this phenomenon deepens our understanding of spin-fluctuation-mediated Cooper pairing, which may be subsequently enhanced by additional interactions such as electron-phonon coupling<sup>23</sup>.

In our opinion, understanding the important role played by AF fluctuations in the superconductivity in NCCO is a prerequisite for any meaningful discussion of spin-fluctuation-mediated pairing in hole-doped cuprates. Specifically, our results here raise the important question of whether a similar gossamer Fermi surface can also exist within the pseudogap of the hole-doped cuprates. If so, the mysterious Fermi arcs and the gossamer Fermi surface near  $(0,\pi)$  may complete the large underlying Fermi surface. More generally, we believe that our study has broader implications and can be applied to deepen our understanding of other electronic-driven superconductors.

# **Online content**

Any methods, additional references, Nature Portfolio reporting summaries, source data, extended data, supplementary information, acknowledgements, peer review information; details of author contributions and competing interests; and statements of data and code availability are available at https://doi.org/10.1038/s41567-023-02209-x.

# References

- Bardeen, J., Cooper, L. N. & Schrieffer, J. R. Theory of superconductivity. *Phys. Rev.* 108, 1175 (1957).
- Scalapino, D. J. The case for d<sub>x</sub><sup>z</sup>-y<sup>z</sup> pairing in the cuprate superconductors. *Phys. Rep.* 250, 329–365 (1995).
- Monthoux, P., Pines, D. & Lonzarich, G. G. Superconductivity without phonons. *Nature* 450, 1177–1183 (2007).
- Scalapino, D. J. A common thread: the pairing interaction for unconventional superconductors. Rev. Mod. Phys. 84, 1383 (2012).
- Wang, F. & Lee, D.-H. The electron-pairing mechanism of iron-based superconductors. Science 332, 200–204 (2011).
- Schrieffer, J. R. Ward's identity and the suppression of spin fluctuation superconductivity. J. Low Temp. Phys. 99, 397–402 (1995).
- Armitage, N. P., Fournier, P. & Greene, R. L. Progress and perspectives on electron-doped cuprates. Rev. Mod. Phys. 82, 2421 (2010).
- Shen, Z.-X. et al. Anomalously large gap anisotropy in the a-b plane of Bi<sub>2</sub>Sr<sub>2</sub>CaCu<sub>2</sub>O<sub>8+5</sub>. Phys. Rev. Lett. 70, 1553 (1993).
- Tsuei, C. C. & Kirtley, J. R. Pairing symmetry in cuprate superconductors. Rev. Mod. Phys. 72, 969 (2000).
- Marshall, D. S. et al. Unconventional electronic structure evolution with hole doping in Bi<sub>2</sub>Sr<sub>2</sub>CaCu<sub>2</sub>O<sub>8+δ</sub>: angle-resolved photoemission results. *Phys. Rev. Lett.* 76, 4841–4844 (1996).
- Loeser, A. G. et al. Excitation gap in the normal state of inderdoped Bi<sub>2</sub>Sr<sub>2</sub>CaCu<sub>2</sub>O<sub>8+δ</sub>. Science 273, 325–329 (1996).
- Ding, H. et al. Spectroscopic evidence for a pseudogap in the normal state of underdoped high-T<sub>c</sub> superconductors. *Nature* 382, 51–54 (1996).

- Timusk, T. & Statt, B. The pseudogap in high-temperature superconductors: an experimental survey. Rep. Prog. Phys. 62, 61–122 (1999).
- Tranquada, J. M., Sternlieb, B. J., Axe, J. D., Nakamura, Y. & Uchida, S. Evidence for stripe correlations of spins and holes in copper oxide superconductors. *Nature* 375, 561–563 (1995).
- Fradkin, E., Kivelson, S. A. & Tranquada, J. Colloquium: theory of intertwined orders in high temperature superconductors. Rev. Mod. Phys. 87, 457 (2015).
- 16. Ghiringhelli, G. et al. Long-range incommensurate charge fluctuations in (Y,Nd)Ba<sub>2</sub>Cu<sub>3</sub>O<sub>6+y</sub>. Science **337**, 821–825 (2012).
- 17. Hashimoto, M. et al. Particle-hole symmetry breaking in the pseudogap state of Bi2201. *Nat. Phys.* **6**, 414–Bi2418 (2010).
- Hinkov, V. et al. Electronic liquid crystal state in the hightemperature superconductor YBa<sub>2</sub>Cu<sub>3</sub>O<sub>6.45</sub>. Science 319, 597–600 (2008).
- Varma, C. M. Non-Fermi-liquid states and pairing instabilities of a general model of copper oxide metals. *Phys. Rev. B* 55, 14554 (1997).
- 20. Markiewicz, R. S. A survey of the Van Hove scenario for high- $T_c$  superconductivity with special emphasis on pseudogaps and striped phases. *J. Phys. Chem. Solids* **58**, 1179–1310 (1997).
- Cuk, T. et al. Coupling of the B<sub>1g</sub> phonon to the antinodal electronic states of Bi<sub>2</sub>Sr<sub>2</sub>Ca<sub>0.92</sub>Y<sub>0.08</sub>Cu<sub>2</sub>O<sub>8+δ</sub>. Phys. Rev. Lett. 93, 117003 (2004).
- Devereaux, T. P., Cuk, T., Shen, Z.-X. & Nagaosa, N. Anisotropic electron-phonon interaction in the cuprates. *Phys. Rev. Lett.* 93, 117004 (2004).
- 23. He, Y. et al. Rapid change of superconductivity and electron-phonon coupling through critical doping in Bi-2212. *Science* **362**, 62–65 (2018).
- 24. Laughlin, R. B. Hartree-Fock computation of the high- $T_c$  cuprate phase diagram. *Phys. Rev. B* **89**, 035134 (2014).
- 25. Thurston, T. R. et al. Antiferromagnetic spin correlations in (Nd, Pr)<sub>2-x</sub>Ce<sub>x</sub>CuO<sub>4</sub>. *Phys. Rev. Lett.* **65**, 263 (1990).
- Matsuda, M. et al. Magnetic order, spin correlations, and superconductivity in single-crystal Nd<sub>1.85</sub>Ce<sub>0.15</sub>CuO<sub>4+δ</sub>. *Phys. Rev. B* 45, 12548 (1992).
- He, J. et al. Fermi surface reconstruction in electron-doped cuprate without antiferromagnetic long-range order. Proc. Natl Acad. Sci. USA 116, 3449–3453 (2019).
- Motoyama, E. M. et al. Spin correlations in the electron-doped high-transition-temperature superconductor Nd<sub>2-x</sub>Ce<sub>x</sub>CuO<sub>4±δ</sub>. Nature 445, 186–189 (2007).
- Armitage, N. P. et al. Anomalous electronic structure and pseudogap effects in Nd<sub>185</sub>Ce<sub>0.15</sub>CuO<sub>4</sub>. Phys. Rev. Lett. 87, 147003 (2001).
- Sénéchal, D. & Tremblay, A.-M. S. Hot spots and pseudogaps for hole- and electron-doped high-temperature superconductors. *Phys. Rev. Lett.* 92, 126401 (2004).
- Onose, Y., Taguchi, Y., Ishizaka, K. & Tokura, Y. Doping dependence of pseudogap and related charge dynamics in Nd<sub>2-x</sub>Ce<sub>x</sub>CuO<sub>4</sub>. Phys. Rev. Lett. 87, 217001 (2001).
- Matsui, H. et al. Angle-resolved photoemission spectroscopy of the antiferromagnetic superconductor Nd<sub>1.87</sub>Ce<sub>0.13</sub>CuO<sub>4</sub>: anisotropic spin-correlation gap, pseudogap, and the induced quasiparticle mass enhancement. *Phys. Rev. Lett.* **94**, 047005 (2005).
- Matsui, H. et al. Evolution of the pseudogap across the magnetsuperconductor phase boundary of Nd<sub>2-x</sub>Ce<sub>x</sub>CuO<sub>4</sub>. *Phys. Rev. B* 75, 224514 (2007).
- 34. Song, D. et al. Electron number-based phase diagram of  $Pr_{1-x}LaCe_xCuO_{4-\delta}$  and possible absence of disparity between electron- and hole-doped cuprate phase diagrams. *Phys. Rev. Lett.* **118**, 137001 (2017).
- 35. Matsui, M. et al. Direct observation of a nonmonotonic  $d_x^z$ - $y^z$ -wave superconducting gap in the electron-doped high- $T_c$  superconductor  $Pr_{0.89}LaCe_{0.11}CuO_4$ . *Phys. Rev. Lett.* **95**, 017003 (2005).

- Armitage, N. P. et al. Superconducting gap anisotropy in Nd<sub>1.85</sub>Ce<sub>0.15</sub>CuO<sub>4</sub>: results from photoemission. *Phys. Rev. Lett.* 86, 1126 (2001).
- 37. Sato, T., Kamiyama, T., Takahashi, T., Kurahashi, K. & Yamada, K. Observation of  $d_x^z$ - $y^z$ -like superconducting gap in an electron-doped high-temperature superconductor. *Science* **291**, 1517–1519 (2001).
- Horio, M. et al. d-wave superconducting gap observed in protect-annealed electron-doped cuprate superconductors Pr<sub>1.3-x</sub>La<sub>0.7</sub>Ce<sub>x</sub>CuO<sub>4</sub>. Phys. Rev. B 100, 054517 (2019).
- Santander-Syro, A. F. et al. Two-Fermi-surface superconducting state and a nodal d-wave energy gap of the electron-doped Sm<sub>1.85</sub>Ce<sub>0.15</sub>CuO<sub>4-δ</sub> cuprate superconductor. *Phys. Rev. Lett.* **106**, 197002 (2011).
- Blumberg, G. et al. Nonmonotonic d<sub>x</sub><sup>z</sup>-y<sup>z</sup> superconducting order parameter in Nd<sub>2-x</sub>Ce<sub>x</sub>CuO<sub>4</sub>. Phys. Rev. Lett. 88, 107002 (2002).
- Yuan, Q., Yuan, F. & Ting, C. S. Nonmonotonic gap in the coexisting antiferromagnetic and superconducting states of electron-doped cuprate superconductors. *Phys. Rev. B* 73, 054501 (2006).
- Lanzara, A. et al. Evidence for ubiquitous strong electron-phonon coupling in high-temperature superconductors. *Nature* 412, 510–514 (2001).
- Park, S. R. et al. Electronic structure of electron-doped Sm<sub>1.86</sub>Ce<sub>0.14</sub>CuO<sub>4</sub>: strong pseudogap effects, nodeless gap, and signatures of short-range order. *Phys. Rev. B* 75, 060501(R) (2007).
- Harter, J. W. et al. Nodeless superconducting phase arising from a strong (π, π) antiferromagnetic phase in the infinite-layer electron-doped Sr<sub>1-x</sub>La<sub>x</sub>CuO<sub>2</sub> compound. *Phys. Rev. Lett.* 109, 267001 (2012).

- Sanders, S. C., Hyun, O. B. & Finnemore, D. K. Specific heat jump at T<sub>c</sub> for Nd<sub>1.85</sub>Ce<sub>0.15</sub>CuO<sub>4-v</sub>. Phys. Rev. B 42, 8035 (1990).
- Park, S. R. et al. Interaction of itinerant electrons and spin fluctuations in electron-doped cuprates. *Phys. Rev. B* 87, 174527 (2013).
- 47. Ishii, K. et al. High-energy spin and charge excitations in electron-doped copper oxide superconductors. *Nat. Commun.* **5**, 3714 (2014).
- Asano, S., Tsutsumi, K., Sato, K. & Fujita, M. Ce-substitution effects on the spin excitation spectra in Pr<sub>1.4-x</sub>La<sub>0.6</sub>Ce<sub>x</sub>CuO<sub>4+δ</sub>. J. Phys. Conf. Ser. 807, 052009 (2017).
- Fujita, M., Matsuda, M., Lee, S.-H., Nakagawa, M. & Yamada, K. Low-energy spin fluctuations in the ground states of electrondoped Pr<sub>1-x</sub>LaCe<sub>x</sub>CuO<sub>4+δ</sub> cuprate superconductors. *Phys. Rev. Lett.* 101, 107003 (2008).
- Yoshida, T. et al. Metallic behavior of lightly doped La<sub>2-x</sub>Sr<sub>x</sub>CuO<sub>4</sub> with a Fermi surface forming an arc. *Phys. Rev. Lett.* 91, 027001 (2002).

**Publisher's note** Springer Nature remains neutral with regard to jurisdictional claims in published maps and institutional affiliations.

Springer Nature or its licensor (e.g. a society or other partner) holds exclusive rights to this article under a publishing agreement with the author(s) or other rightsholder(s); author self-archiving of the accepted manuscript version of this article is solely governed by the terms of such publishing agreement and applicable law.

© The Author(s), under exclusive licence to Springer Nature Limited 2023

<sup>1</sup>Stanford Institute for Materials and Energy Sciences, SLAC National Accelerator Laboratory, Menlo Park, CA, USA. <sup>2</sup>Geballe Laboratory for Advanced Materials, Stanford University, Stanford, CA, USA. <sup>3</sup>Department of Applied Physics, Stanford University, Stanford, CA, USA. <sup>4</sup>Department of Applied Physics, KTH Royal Institute of Technology, Stockholm, Sweden. <sup>5</sup>Stanford Synchrotron Radiation Lightsource, SLAC National Accelerator Laboratory, Menlo Park, CA, USA. <sup>6</sup>Beijing National Laboratory for Condensed Matter Physics and Institute of Physics, Chinese Academy of Sciences, Beijing, China. <sup>8</sup>Department of Physics and CAS Key Laboratory of Strongly-Coupled Quantum Matter Physics, University of Science and Technology of China, Hefei, China. <sup>9</sup>Department of Applied Physics, Yale University, New Haven, CT, USA. <sup>10</sup>Department of Materials Science and Engineering, Stanford University, Stanford, CA, USA. <sup>11</sup>Department of Physics, Stockholm University, Stockholm, Sweden. <sup>12</sup>Department of Physics, University of California, Berkeley, CA, USA. <sup>13</sup>Material Sciences Division, Lawrence Berkeley National Laboratory, Berkeley, CA, USA. <sup>14</sup>Department of Physics, Stanford University, Stanford, CA, USA. <sup>15</sup>Present address: Department of Physics, University of California, Berkeley, CA, USA. <sup>16</sup>These authors contributed equally: Ke-Jun Xu, Qinda Guo, Makoto Hashimoto, Zi-Xiang Li. ⋈e-mail: dunghai@berkeley.edu; oscar@kth.se; zxshen@stanford.edu

#### Methods

#### Sample synthesis and annealing

 $Nd_{2-x}Ce_xCuO_4$  (NCCO) single crystals were grown with the travelling-solvent floating zone method with CuO flux in the molten zone. The crystals were annealed at 900 °C under flowing Ar gas and were optimized to obtain the highest and sharpest superconducting transition:  $T_c \approx 25 \, \text{K}$  and  $\Delta T_c \approx 2 \, \text{K}$ . The  $T_c$  values of the samples were characterized in a physical property measurement system using the a.c. susceptibility method. We note that here the onset of diamagnetism is taken as  $T_c$ , as that is usually the temperature at which the resistivity reaches 0. The width of the transition  $\Delta T_c$  is defined here as the temperature range over which the magnetization drops from 90% to 10%. The Ce content of the crystals was characterized by wavelength-dispersive spectroscopy in an electron probe microanalyser.

#### **ARPES** measurements

The ARPES measurements were performed at the Bloch beamline (MAX IV) and beamline 5-4 (Stanford Synchrotron Radiation Lightsource (SSRL)). Preliminary measurements were also carried out at beamline 5-2 (SSRL). Single-crystal NCCO samples were mounted on top of copper posts with H20E silver epoxy and Torr Seal. Laue backscattering was performed to align the sample in the basal plane. A ceramic top post was mounted with Torr Seal for in situ cleaving. Here 16.5 eV photons were used to obtain an adequate zone boundary intensity and maintain a low photon energy for good energy resolutions. The beam spot size is estimated to be around 30 μm × 18 μm at MAX IV and about 100 μm × 150 μm at SSRL beamline 5-4. The  $E_{\rm F}$  value is measured on reference polycrystal gold and carefully checked for extrinsic sample charging and space charging effects for the superconducting gap measurements. During the superconducting gap measurements at SSRL beamline 5-4,  $E_{\rm F}$  is generally measured about every 30–45 min to account for a slow drift in the photon energy on the scale of <0.5 meV h<sup>-1</sup> due to monochromator warm up and diurnal variations. We note that once the beamline reaches a stable state, the drift is usually about 0.1 meV h<sup>-1</sup> or less. The experimental resolution for the superconducting gap measurements is about 4 meV and is determined from fitting the Fermi cutoff of the reference gold.

We find that a number of factors work in concert to enable the measurement of high-quality spectra and the observation of the Bogoliubov quasiparticle in the electron-doped cuprates.

- 1. We have synthesized and annealed high-quality NCCO crystals that show  $T_{\rm c}$  (defined by the onset of magnetization drop, usually comparable with when the resistivity reaches 0) of 25–26 K and transition width of around 2 K. A high  $T_{\rm c}$  and narrow transition width, indicative of high crystal quality and uniformity, are required for observing the Bogoliubov quasiparticles.
- The measurement photon energy selection is important for achieving high counts without compromising the measurement resolution (through effects such as space charging). A high-flux, tunable and highly monochromatic light source, such as beamline 5-4 at SSRL or Bloch beamline (MAX IV), is required for this measurement.
- 3. For the superconducting gap measurements, a light source with high energy resolution and high stability is required. We find that the typical photon energy drift (>1–2 meV h<sup>-1</sup>) at most beamlines is not suitable for the superconducting gap measurements on the electron-doped cuprate superconductors, due to the relatively low counts of the valence electrons in the cuprates and therefore the long data acquisition times required.
- 4. During the temperature-dependent measurements, excellent control of the vacuum at different temperatures is required. For beamline 5-4 at SSRL, we have implemented a local heater that controls the sample temperature without disturbing the

- temperature of the entire manipulator arm. This way, outgassing during temperature cycling is minimized and the measurement chamber vacuum is kept below  $2.5 \times 10^{-11}$  torr at all times.
- 5. For an improved signal-to-noise ratio, the metal mesh in front of the multichannel plate detector at beamline 5-4 of SSRL is removed. Due to the excellent vacuum conditions and mu-metal shielding on the chamber, the mesh that is used to suppress ion feedback noise and shield magnetic fields has minimal benefits.
- 6. Unlike the commonly studied hole-doped cuprate Bi<sub>2</sub>Sr<sub>2</sub>Ca-Cu<sub>2</sub>O<sub>8</sub> that is flaky with a van der Waals BiO–BiO interface, the *T'* electron-doped cuprates are rock like and difficult to cleave. To obtain flat cleavage surfaces that show step-like terraces, special cleaving geometries are required. Here the sample is first shaped into an elongated rectangle, with the long direction along the *c* axis. Then, Torr Seal is applied with the top ceramic post such that the epoxy covers large portions of the sides of the crystal. This way, the cleaving process applied a uniform fracture force along a small cross section and is more likely to generate a high-quality cleave.
- 7. Even with the above cleaving method, there may be areas of the cleaved surface that have a rugged terrain, which do not produce high-quality ARPES spectra. A small beam spot combined with spatial photoemission scanning capabilities are required to seek out high-quality cleaved spots. For the gap measurements at beamline 5-4 with a slightly larger beam spot, multiple cleaves are usually needed to find a cleaved surface with a larger area of high-quality surface.

#### **ARPES data processing**

To properly process the raw data to the presented data in the figures, several careful calibrations and conversions are required. Standard ARPES data processing procedures  $^{51,52}$  were performed, including detector-channel inhomogeneity calibration, detector nonlinearity calibration, analyser slit inhomogeneity and lensing calibration;  $E_F$  calibration with respect to an electrically connected polycrystalline gold reference; and emission-angle-to-momentum conversion. Normalizations of ARPES spectral intensities are performed using the high-order light background intensity above  $E_F$ , well above any significant thermal tail of the Fermi–Dirac distribution. To remove the incoherent scattering background, a reference EDC background far away from dispersive features is subtracted from the spectra.

# Phenomenological fitting of the superconducting gap

The superconducting gap is fitted using the phenomenological model presented elsewhere<sup>53</sup>, where the self-energy in the superconducting state has the following form.

$$\Sigma(\mathbf{k},\omega) = -i\Gamma_1 + \frac{\Delta^2}{\omega + \epsilon(\mathbf{k}) + i\Gamma_0}$$

Here  $\Gamma_1$  is the single-particle scattering rate and  $\Delta$  is the gap magnitude. We note that due to the large energy scale of the AF gap compared with the superconducting gap, the inverse-pair lifetime i $\Gamma_0$ , used to account for the pseudogap on the hole-doped side, can be taken as 0 at temperatures markedly below  $T_c$  when modelling the low-energy superconducting peak in NCCO. For the temperature-dependent EDC fittings, the pair-breaking term is left as a free parameter.

## Spin orientation fluctuation calculations

The AF order parameter is a three-component vector. It has a modulus  $\rho_{AF}$  and orientation  $\hat{n}$ , namely,  $\vec{N} = \rho_{AF}\hat{n}$ . This is analogous to the superconducting order parameter that has a modulus and a phase, namely,  $\rho_{SC}e^{i\theta}$ . In the latter case, the superconducting-gap-opening temperature marks the onset of non-zero  $\rho_{SC}$ , whereas the phase

coherence temperature marks the onset of  $\langle e^{i\theta} \rangle \neq 0$  (and the vanishing of resistivity). Similarly, in an antiferromagnet, the onset of non-zero  $\rho_{AF}$  signals the opening of the AF gap. However, because the AF order occurs at non-zero momentum, non-zero  $\rho_{AF}$  generically only partially gaps the Fermi surface (unless there is nesting). However, even when  $\rho_{AF}$  is non-zero, the presence of AF long-range order depends on whether  $\hbar$  is ordered.

In view of the experimental data, we realize that in an AF system with non-zero  $\rho_{\rm AF}$  but with disordered  $\hat{n}$ , the Fermi surface can be restored due to orientation fluctuations. Our theoretical treatment assumes that the orientation fluctuations are slow compared with the photoemission timescale; hence, we view the measured photoemission spectra as taking snapshots of the electronic structure under different orientation configurations and then average over these configurations. This is analogous to the Born–Oppenheimer approximation used to treat phonons. In addition, we treat the breakdown of this approximation as causing Cooper pairing just as in the electron–phonon interaction problem.

Our calculation is done with a tight-binding model that fits the high-temperature photoemission data. The tight-binding Hamiltonian is given by

$$H_0 = \sum_{i,l,\sigma} \left( -t_{ij} c_{i\sigma}^+ c_{j\sigma} + \text{h.c.} \right) - \mu \sum_{i\sigma} c_{i\sigma}^+ c_{i\sigma},$$

where for the nearest-neighbour/second-nearest-neighbour hopping,  $t_{ij}=0.3260/-0.0766$  eV; the chemical potential  $\mu$  is taken to be -0.0400 eV. We then set  $\rho_{\rm AF}$  by demanding the zero-temperature AF gap at the hot spot be approximately equal to that measured in ARPES (-0.1 eV). Subsequently, we generate a set of orientation ( $\hat{n}$ ) configurations, using a two-dimensional classical Heisenberg model as the Boltzmann weight. The Hamiltonian in the presence of the fluctuating AF order parameters is given by

$$H = H_0 + \rho_{AF} \sum_{i,\alpha,\beta} (-1)^i c_{i\alpha}^+ \left( \hat{n}_i \cdot \vec{\sigma}_{\alpha\beta} \right) c_{i\beta}.$$

Here  $(-1)^i$  is the staggered factor associated with AF,  $\vec{\sigma}$  are the Pauli matrices and  $\alpha$ ,  $\beta$  = x, y, z. We characterize each set of configuration by its orientation correlation length  $\xi_{AF}$  (which is controlled by the coupling strength that enters the Heisenberg model). Since we need to compute the electron spectral function under an arbitrary orientation configuration, such a calculation needs to be numerically carried out on an  $L \times L$  lattice ( $L_{max}$  = 100 for Fermi surface mapping and 60 in the energy-momentum cuts). We broaden the discrete energy levels at finite L by an energy-dependent factor  $\Gamma(E)$  = 0.002 eV + 0.4 × E. The results associated with different configurations are then averaged over 2400 orientation configurations. To study superconducting pairing, after integrating out the fast orientation fluctuation, we assume that a short-range AF interaction is generated, which causes Cooper pairing. Cooper pairing is implemented in real space by a nearest-neighbour d-wave pairing with pairing amplitude  $\Delta_{ij}$  = 0.01 eV.

#### Phase separation is an unlikely origin of in-gap states

Doping and magnetic phase separation could produce regions of AF order and superconductivity. The resulting ARPES spectra may present as a combination of reconstructed and unreconstructed Fermi surface. In the following, we present arguments disfavouring the coexistence of metallic spatial regions and AF spatial regions with different doping densities being the primary factor governing the behaviour observed.

 Analysis of the momentum distribution curves near the hot spot shows that the dispersions of the high- and low-energy states are consistent with the same doping (Extended Data Fig. 7), thereby excluding significant doping inhomogeneity.

- 2. Neutron scattering results<sup>54</sup> of NCCO at the same doping level revealed a spin gap at low energies and temperatures. Moreover, there is no evidence of spin excitations below the spin gap within the experimental resolution. This indicates that there are no significant spatial regions where there is a well-defined AF order.
- Field-dependent neutron scattering results<sup>55</sup> show that dynamical magnetic correlations are long-ranged, spanning vortex cores and superconducting regions. This implies that the magnetic fluctuations are uniform at the scale of the superconducting coherence length.
- 4. Cu nuclear magnetic resonance results<sup>56</sup> show a lack of low-temperature wipeout effect in the closely related compound Pr<sub>1.85</sub>Ce<sub>0.15</sub>CuO<sub>4</sub>, indicating that there is no slowing down of the spins at low temperatures. Since the nuclear magnetic resonance signal is sensitive to the local magnetic field, this result suggests that as far as magnetism is concerned, the sample appears homogeneous.
- 5. In the scenario of mesoscopic phase separation, it is the volume fraction that changes as a function of doping, rather than the chemical potential. However, the chemical potential continuously shifts with doping in NCCO (ref. 57), indicating that phase separation is not significant.

#### **Specific heat measurements**

Specific heat measurements were carried out in a differential membrane-based nanocalorimeter <sup>58</sup> at Stockholm University. A small piece of the sample was broken off from the larger crystals used for the ARPES studies and mounted with Apiezon grease. The background of the empty cell and grease were calibrated. A magnetic field was used to push the specific heat to jump from around 25 K to a lower temperature, such that the zero-magnetic-field jump magnitude can be detected from the difference between the zero-field and finite-field curves (Extended Data Fig. 6). The absolute value of the molar specific heat was estimated from the magnitude of the low-temperature Nd moment Schottky anomaly signal.

# Expected specific heat jump from band structure

The electronic specific heat is related to the density of states through

$$C_{\rm e} = \frac{\partial S_{\rm e}}{\partial T}$$

where  $S_e$  is the quasiparticle entropy:

$$S_{\rm e} = k_{\rm B} \int \left[ -f \ln f - \left( 1 - f \right) \ln \left( 1 - f \right) \right] D(E) \, \mathrm{d}E,$$

Here  $k_B$  is the Boltzmann constant, f is the Fermi–Dirac function and D(E) is the quasiparticle density of states. Here D(E) can be calculated from the tight-binding band parameter by integrating the states near the Fermi level in momentum space:

$$D(E) = \frac{1}{4\pi^3} \int_{FS} \frac{\mathrm{d}k}{\partial E(k)}.$$

Extended Data Fig. 6 shows the results for the Sommerfeld coefficient  $\gamma$ , or C/T, for NCCO and  $La_{2-x}Sr_xCuO_4$  using the tight-binding parameters for NCCO and  $La_{2-x}Sr_xCuO_4$ , respectively. Here, as the presence of the AF reconstruction affects the measured dispersion in underdoped and optimally doped NCCO, the bare-band tight-binding parameters are approximated by the overdoped side where the effect of AF is minimal. The tight-binding parameters used for the density of states calculations here are  $\mu = -0.065$ , t = 0.2497 and t' = -0.1036, extracted from the heavily surface-dosed spectra (similar to that in

Extended Data Fig. 4). Using the parameters from a different doping level is justified for the bare-band expectation as the density of states does not vary much in this doping regime, such that a slight shift in the doping, and therefore the chemical potential level, minimally affects the electronic y value.

This result does not take into consideration the AF pseudogap and reconstruction, which may partially gap out states and affect the actual density of states. By comparing the expected specific anomaly  $\Delta C/T$  of the bare band with the experimental value, one can estimate the effects of the AF pseudogap. At x=0.15, the calculated y is about 2.6 mJ mol K<sup>-2</sup> (Extended Data Fig. 8). Combined with the BCS expectation for a d-wave superconductor, we get <sup>59,60</sup>

$$\Delta C_{\rm BCS}/T = 1.43\gamma$$
.

The tight-binding band-specific anomaly is estimated to be about 3.7 mJ mol K $^2$ . Compared with the measured experimental  $\Delta C/T$  value of 1.2 mJ/mol K $^2$  (Extended Data Fig. 6), the calculated  $\Delta C_{\rm BCS}/T$  is more than twice as large, indicating that a notable portion of the spectral weight is missing in the superconducting transition. We have also calculated y using the x = 0.15 fitted tight-binding parameters ( $\mu$  = -0.04, t = 0.326 and t' = -0.0766), which includes renormalization effects from AF but not spectral-weight suppression. This method produces about 3.1 mJ mol K $^2$  at 15% doping, still appreciably larger than the experimentally measured value of 1.2 mJ mol K $^2$ .

## **Data availability**

The data presented in this work are available via the Stanford Digital Depository at https://purl.stanford.edu/gt676zx4703. Source data are provided with this paper.

#### References

- Sobota, J., He, Y. & Shen, Z.-X. Angle-resolved photoemission studies of quantum materials. Rev. Mod. Phys. 93, 025006 (2021).
- Chen, S.-D. High Precision Photoemission Study of Overdoped Bi2212 Superconductors. PhD thesis, Stanford Univ. (2021).
- Norman, M. R., Randaria, M., Ding, H. & Campuzano, J. C. Phenomenology of the low-energy spectral function in high-T<sub>c</sub> superconductors. *Phys. Rev. B* **57**, R11093(R) (1998).
- Yamada, K. et al. Commensurate spin dynamics in the superconducting state of an electron-doped cuprate superconductor. *Phys. Rev. Lett.* **90**, 137004 (2003).
- Motoyama, E. M. et al. Magnetic field effect on the superconducting magnetic gap of Nd<sub>1.85</sub>Ce<sub>0.15</sub>CuO<sub>4</sub>. Phys. Rev. Lett. 96, 137002 (2006).
- Williams, G. V., Hasse, J., Park, M.-S., Kim, K. H. & Lee, S.-I. Doping-dependent reduction of the Cu nuclear magnetic resonance intensity in the electron-doped superconductors. *Phys. Rev. B* 72, 212511 (2005).
- Harima, N. et al. Chemical potential shift in Nd<sub>2-x</sub>Ce<sub>x</sub>CuO<sub>4</sub>: contrasting behavior between the electron- and hole-doped cuprates. *Phys. Rev. B* 64, 220507(R) (2001).
- Tagliati, S., Krasnov, V. M. & Rydh, A. Differential membrane-based nanocalorimeter for high-resolution measurements of lowtemperature specific heat. Rev. Sci. Instrum. 83, 055107 (2012).
- Loram, J. W., Luo, J., Cooper, J. R., Liang, W. Y. & Tallon, J. L.
   Evidence on the pseudogap and condensate from the electronic specific heat. J. Phys. Chem. Solids 62, 59–64 (2001).
- Williams, P. J. & Carbotte, J. P. Specific heat of a d-wave superconductor stabilized by antiferromagnetic fluctuations. *Phys. Rev. B* 39, 2180 (1989).

# **Acknowledgements**

We thank S. A. Kivelson, L. Taillefer, Y. Wang, B. Moritz and Y. Zhong for fruitful discussions. Technical assistance and valuable discussions with C. Polly, B. Thiagarajan and H. Fedderwitz are gratefully acknowledged. The work at Stanford University and Stanford Institute for Materials and Energy Sciences is supported by the Department of Energy, Office of Basic Energy Sciences, Division of Materials Sciences and Engineering, under contract DE-AC02-76SF00515 (K.-J.X., M.H., S.-D.C., J.H., Y.H., C.L., C.R.R., Y.S.L., T.P.D., D.-H. Lu and Z.-X.S.). Use of the Stanford Synchrotron Radiation Lightsource, SLAC National Accelerator Laboratory, is supported by the US Department of Energy, Office of Science, Office of Basic Energy Sciences, under contract no. DE-ACO2-76SF00515 (K.-J.X., D.-H. Lu, M.H., S.-D.C., J.H., Y.H. and Z.-X.S.), Z.-X.S. acknowledges the hospitality of KTH and the Swedish Research Council during his sabbatical, when this collaboration started. We acknowledge MAX IV Laboratory for time on the Bloch beamline under Proposal 20210256 (Q.G., C.L., M.H.B. and O.T.). Research conducted at MAX IV, a Swedish national user facility, is supported by the Swedish Research Council under contract 2018-07152, the Swedish Governmental Agency for Innovation Systems under contract 2018-04969 and Formas under contract 2019-02496. The work at KTH and MAX IV was supported by Swedish Research Council grants 2019-00701 and 2019-03486, as well as The Knut and Alice Wallenberg Foundation grant 2018.0104 (Q.G., C.L., M.H.B. and O.T.). D.-H. Lee was funded by the US Department of Energy, Office of Science, Office of Basic Energy Sciences, Materials Sciences and Engineering Division, under contract no. DEACO2-05-CH11231 (Quantum Material Program KC2202). Y.H. acknowledges support from the NSF CAREER award no. DMR-2239171.

# **Author contributions**

K.-J.X., M.H., O.T. and Z.-X.S. conceived the experiment. K.-J.X., J.H., C.R.R. and Y.S.L. synthesized the samples. K.-J.X., M.H. and D.-H. Lu performed the ARPES measurements at SSRL. Q.G., C.L. and M.H.B. performed the ARPES measurements at MAX IV. A.R. performed the specific heat measurements. K.-J.X., Q.G., M.H., S.-D.C., Y.H., T.P.D., D.-H. Lee, O.T. and Z.-X.S. analysed and interpreted the ARPES data. Z.-X.L. and D.-H. Lee conceived the theoretical model and performed the numerical calculations. K.-J.X., M.H., D.-H. Lee and Z.-X.S. wrote the manuscript with input from all authors.

#### **Competing interests**

The authors declare no competing interests.

## **Additional information**

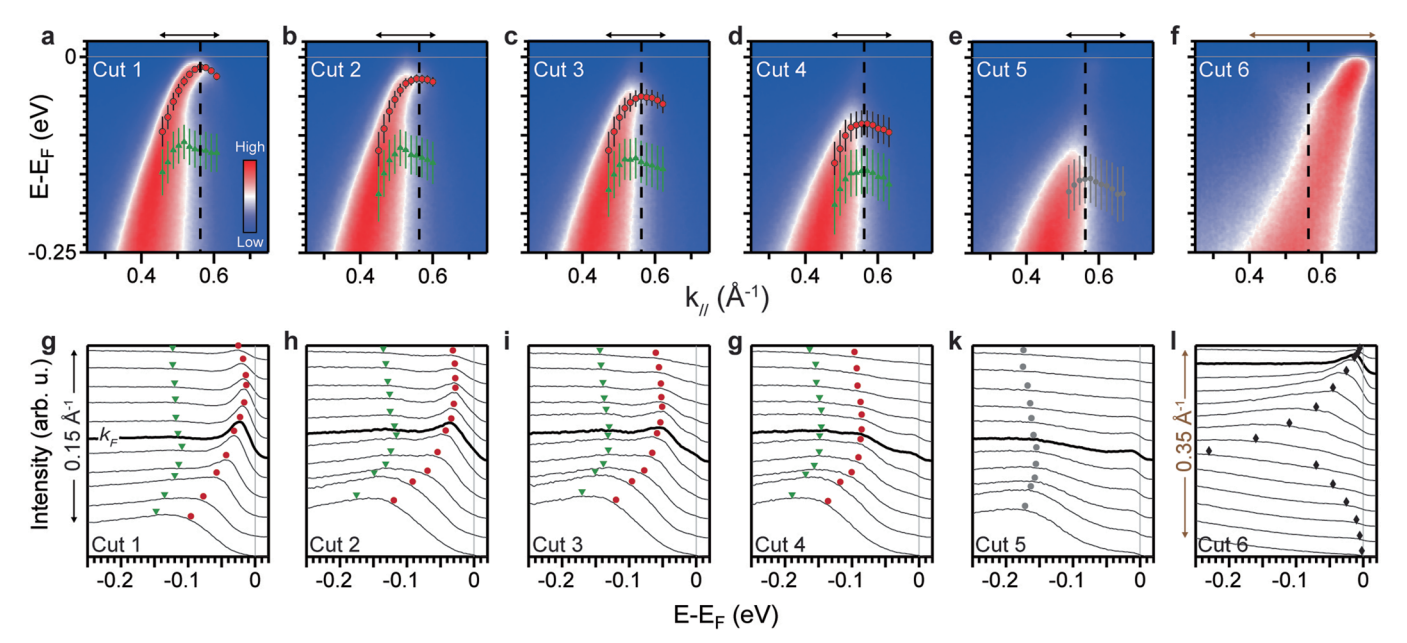
**Extended data** is available for this paper at https://doi.org/10.1038/s41567-023-02209-x.

**Supplementary information** The online version contains supplementary material available at https://doi.org/10.1038/s41567-023-02209-x.

**Correspondence and requests for materials** should be addressed to Dung-Hai Lee, Oscar Tjernberg or Zhi-Xun Shen.

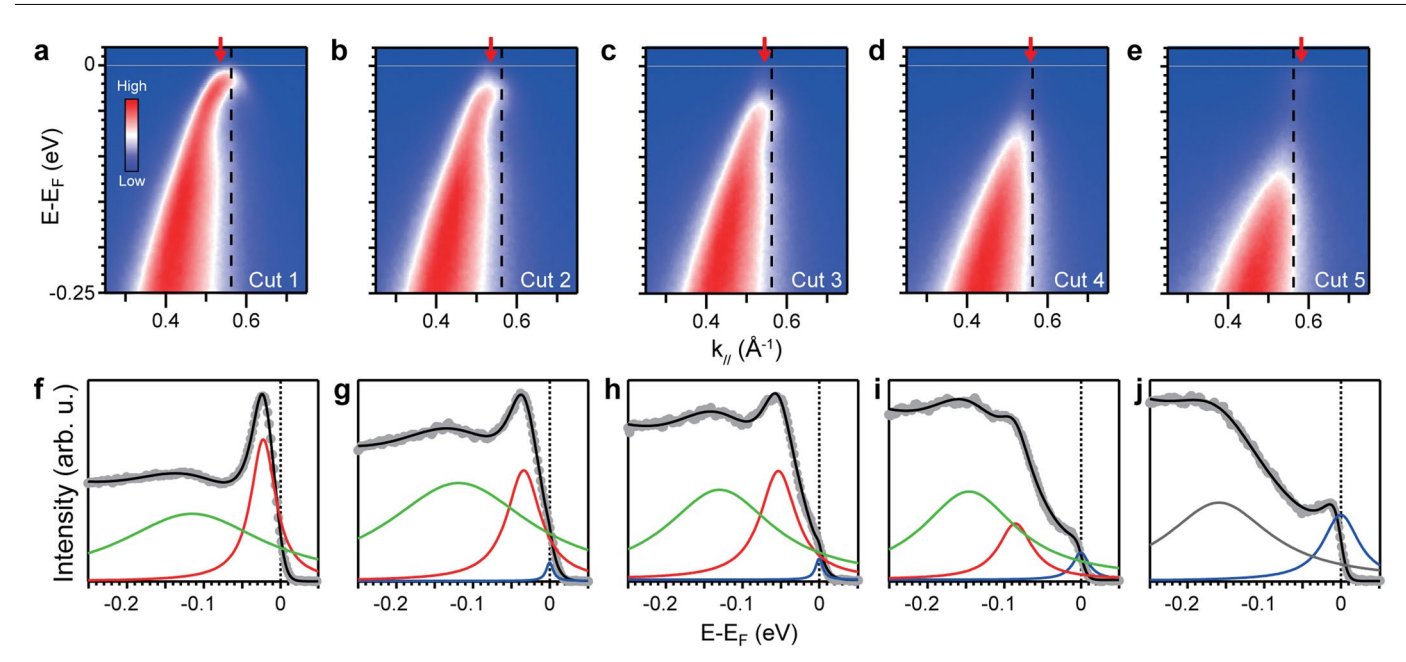
**Peer review information** *Nature Physics* thanks Thomas Maier and the other, anonymous, reviewer(s) for their contribution to the peer review of this work.

**Reprints and permissions information** is available at www.nature.com/reprints.



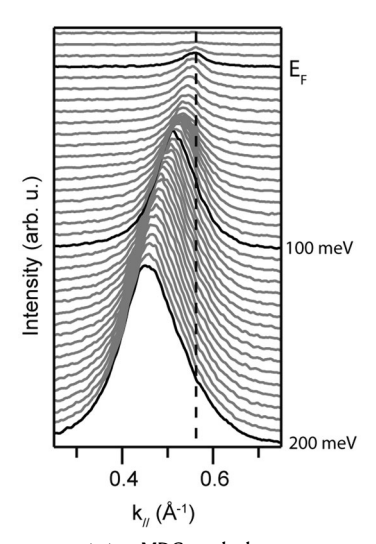
Extended Data Fig. 1 | Energy distribution curves of the normal-state spectra in  $Nd_{1.85}Ce_{0.15}CuO_4$ . a-f, energy-momentum spectra from the corresponding cuts 1–6 in main Fig. 1g. Red dots track the position of the peak associated with AF and green triangles track a higher energy hump feature (see main text). Grey dots in (e) track the only observable broad feature in this cut. Vertical black dashed line indicates the AF zone boundary. Grey line indicates the Fermi energy  $E_{\rm F}$  Error

bars correspond to the width of peaks in Energy distribution curve (EDC) fittings. g-I, EDCs of the momentum region indicated by the black double arrows in the respective cuts in a-f. Red, green, and grey dots indicate the same respective features as a-f. Black diamonds in I indicates the zone boundary dispersion and reconstructed electron pocket. The thick black line indicates the Fermi momentum  $k_F$ , and the grey vertical line indicates  $E_F$ .

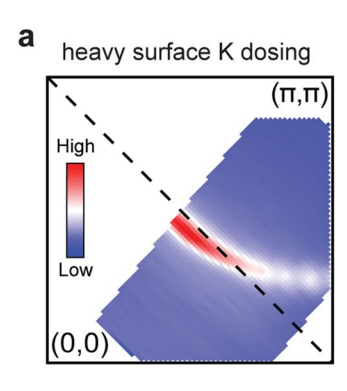


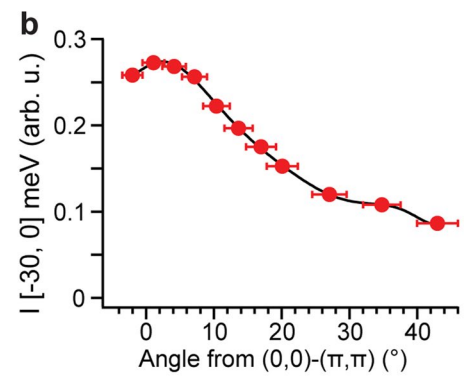
Extended Data Fig. 2 | Spectral fittings in the normal state spectra. a-e, Normal spectra for cuts 1-5 that are the same as that in main Fig. 1. Small red arrow points to the Fermi momentum. f-j, Fits of the EDC curves. Grey dots are

the raw  $k_F$  EDC data, with the fittings shown by the overlaying black curve. The EDCs are fitted with 3 Lorentzian in  $\mathbf{g}$ – $\mathbf{i}$  and 2 Lorentzian for  $\mathbf{f}$  and  $\mathbf{j}$ . Each fit is also convolved with the Fermi-Dirac function.



 $\textbf{Extended Data Fig. 3} | \textbf{Momentum distribution curves of gossamer states.} \ \textbf{MDCs} \ at the hot spot, same as cut 4 in the main text Fig. 1, showing peaks within the AF pseudogap (which has a broad gap edge at around 100 meV). The dispersion of the gossamer states is extracted by fitting the MDC peaks with Lorentzian peaks.$ 

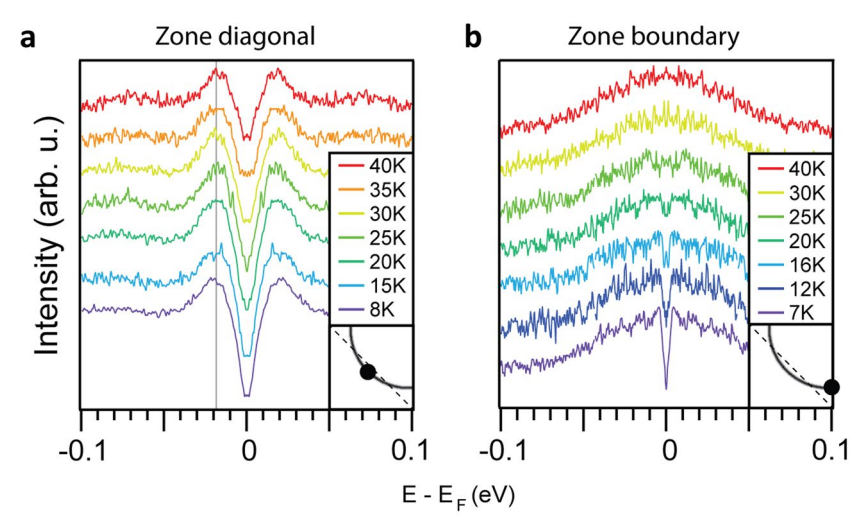




# $\textbf{Extended Data Fig. 4} \\ \textbf{Momentum-dependent matrix element normalization.}$

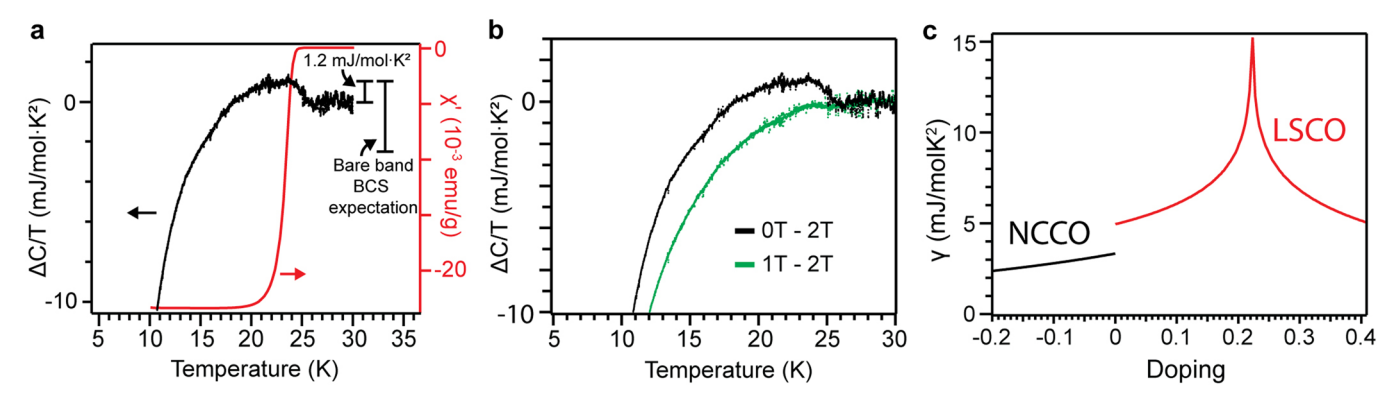
 $\label{eq:approx} \textbf{a}, \text{Fermi surface mapping of an NCCO sample where the surface was heavily dosed with K atoms, such that there are no visible AF spectral signatures.}$   $\textbf{b}, \text{angular dependence of the } k_F \text{ spectral weight of the surface-K-dosed sample}$ 

(red dots) as in a. The black curve is a high order polynomial fit to extract the angle-dependent normalization factor. Horizontal error bars correspond to the uncertainty in the absolute momentum determination.



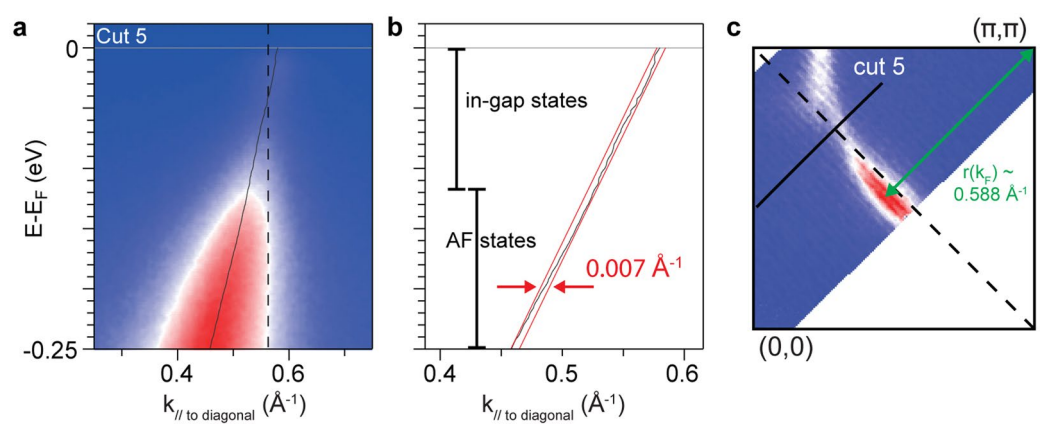
Extended Data Fig. 5 | Temperature dependence of Brillouin zone diagonal and Brillouin zone boundary spectra for  $Nd_{1.85}Ce_{0.15}CuO_4$ , a, b, Temperature dependence of the  $k_F$  EDCs at the Brillouin zone diagonal (a) and Brillouin zone boundary (b), with Brillouin zone position shown in the respective insets.

Measurement temperatures are indicated by the colored legends. The grey vertical line in (a) is a guide to the eye highlighting the persistence of the AF feature through the superconducting transition temperature of 25 K.



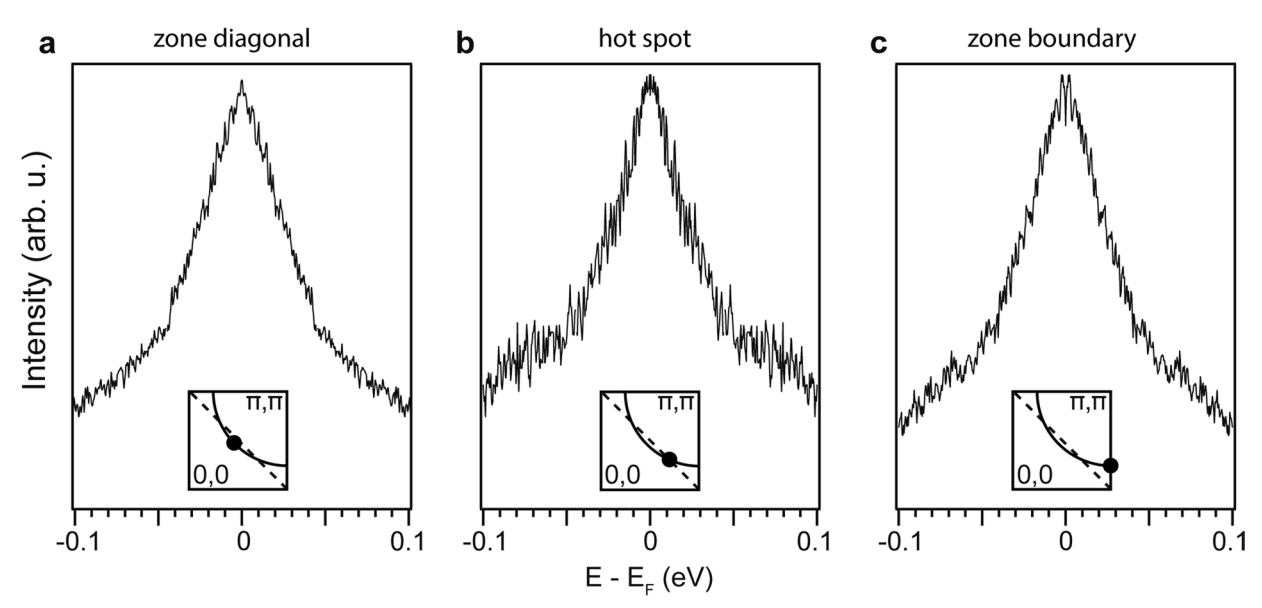
**Extended Data Fig. 6 | Specific heat reveals small superconducting transition anomaly. a**, Difference specific heat (left) and magnetic susceptibility (right) as a function of temperature. The difference specific heat is extracted by subtracting the zero field curve by the 2T curve. The low temperature drop off is from the field dependence of the Nd Schottky anomaly. The bare band expectation based on Bardeen-Cooper-Schrieffer (BCS) theory is derived from the calculated electronic specific heat in **c. b**, comparison of the zero field and

finite field C/T curves for extraction of the electronic specific heat. 2T is enough to suppress the transition to a lower temperature such that the full height of the jump is preserved in the difference curve.  $\mathbf{c}$ , Calculated electronic specific heat from the bare band tight binding parameters, for NCCO (black curve) and LSCO (red curve). See Methods sections VII and VIII for additional information of the electronic specific heat calculation and derivation of the expected BCS specific heat jump size.



**Extended Data Fig. 7** | **Excluding significant doping inhomogeneity. a**, ARPES spectra of cut 5 in Fig. 1. Diagonal black line is the dispersion extracted from fitting the momentum distribution curves (MDCs). **b**, Dispersion extracted from MDC fitting. The red lines are bounds on the momentum deviation of the dispersion. **c**, Fermi surface mapping constructed using intensity from  $\pm 10$  meV of  $E_F$ . Green line indicates the approximate radius of the large Fermi pocket. We can place an upper bound on the doping uncertainty by the momentum bounds in **b**. Here, the effect of the AF reconstruction is broad enough to facilitate the extraction of an approximately linear dispersion in this energy range. The intensity between  $E_F$  and  $E_B - 100$  meV is from the in-gap residual states, and the intensity at  $E_B > -100$  meV is dominated by the AF states. If the AF and in-gap states originate from distinct doping regions, then we expect the dispersions of the

in-gap states and AF states to be offset in momentum. The deviation from a linear dispersion is bounded to be about  $\Delta k \sim 0.007\, \text{Å}^{-1}$ . We note that while the individual MDC widths are larger than this momentum uncertainty, the collective noise in the dispersion fittings show an error smaller than  $\Delta k \sim 0.007\, \text{Å}^{-1}$ . This momentum uncertainty can be translated to a Fermi surface volume uncertainty by the following approximation  $\Delta A_{FS} \sim 2\pi r (k_F) \cdot \Delta k = 0.025 \pm 0.003\, \text{Å}^{-2}$ , where  $r(k_F)$  is the approximate radius of the large Fermi surface that is nearly circular in this doping regime. We note that the uncertainty in  $r(k_F)$ , which we use a generous estimate of  $\pm 0.05\, \text{Å}^{-1}$ , is about  $\pm 10\%$  and linearly affects  $\pm 20\%$ . The doping uncertainty is the  $\pm 20\%$  and  $\pm 20\%$  from the nominal  $\pm 20\%$  doping), and thus excludes significant doping phase separation in our measured samples.



**Extended Data Fig. 8** | **Symmetrized spectra in overdoped sample reached by surface K dosing. a–c,** symmetrized EDC at the zone diagonal (a), hot spot (b), and zone boundary (c)  $k_F$ . The momentum location of the EDC is shown in the respective insets. Here, little to no signature of the incipient antiferromagnetic gap is observed anywhere in momentum. No superconducting gap is observed within the experimental temperature and resolution. We note that while the

experimental resolution is -4 meV, this number is defined by the broadening of the Fermi Dirac cutoff, and typically one can observe gap features much smaller than the experimental resolution. Here, the extremely overdoped side is reached via surface K dosing, which introduces additional electrons into the system. From the Fermi surface volume, we estimate the doping to be about 19%.